



Supporting Online Material for

## The Detection of a Population of Submillimeter–Bright, Strongly-Lensed Galaxies

Mattia Negrello,\* R. Hopwood, G. De Zotti, A. Cooray, A. Verma, J. Bock, D. T. Frayer, M. A. Gurwell, A. Omont, R. Neri, H. Dannerbauer, L. L. Leeuw, E. Barton, J. Cooke, S. Kim, E. da Cunha, G. Rodighiero, P. Cox, D. G. Bonfield, M. J. Jarvis, S. Serjeant, R. J. Ivison, S. Dye, I. Aretxaga, D. H. Hughes, E. Ibar, F. Bertoldi, I. Valtchanov, S. Eales, L. Dunne, S. P. Driver, R. Auld, S. Buttiglione, A. Cava, C. A. Grady, D. L. Clements, A. Dariush, J. Fritz, D. Hill, J. B. Hornbeck, L. Kelvin, G. Lagache, M. Lopez-Caniego, J. Gonzalez-Nuevo, S. Maddox, E. Pascale, M. Pohlen, E. E. Rigby, A. Robotham, C. Simpson, D. J. B. Smith, P. Temi, M. A. Thompson, B. E. Woodgate, D. G. York, J. E. Aguirre, A. Beelen, A. Blain, A. J. Baker, M. Birkinshaw, R. Blundell, C. M. Bradford, D. Burgarella, L. Danese, J. S. Dunlop, S. Fleuren, J. Glenn, A. I. Harris, J. Kamenetzky, R. E. Lupu, R. J. Maddalena, B. F. Madore, P. R. Maloney, H. Matsuhara, M. J. Michaowski, E. J. Murphy, B. J. Naylor, H. Nguyen, C. Popescu, S. Rawlings, D. Rigopoulou, D. Scott, K. S. Scott, M. Seibert, I. Smail, R. J. Tuffs, J. D. Vieira, P. P. van der Werf, J. Zmuidzinas

\*To whom correspondence should be addressed E-mail: m.negrello@open.ac.uk

Published 5 November 2010, *Science* **330**, 800 (2010)

DOI: 10.1126/science.1193420

### This PDF file includes:

SOM Text

Figs. S1 to S9

Tables S1 to S4

References

# Supporting Online Material

## MAMBO observations

The five H-ATLAS/SDP lens candidates, i.e. ID9, ID11, ID17, ID81 and ID130, were observed on 2010 March 9 and 10, with MAMBO, at the IRAM 30 meter telescope on Pico Veleta, in Director's Discretionary Time (DDT). The MAMBO array consists of 117 bolometer elements and operates at a central frequency of 250 GHz, corresponding to 1.2 mm. The beam size (FWHM  $\approx$  11 arcsec) of MAMBO ensures that the true dust emission at 1.2 mm is obtained if the source is not more extended than a few arcseconds. Each science target was observed in the photometric mode ("on-off") of MAMBO which is based on the chop-nod technique and placing the target on a reference bolometer element (on-target channel). The total observing time was 1.5 hours. Data were reduced using MOPSIC, and the current version of MOPSI (Zylka 1998, The MOPSI Cookbook (Bonn: MPIfR)).

## Keck observations

The imaging observations were acquired on 10 March 2010 using the dual-arm Low Resolution Imaging Spectrometer [LRIS; (1, 2)] on the 10-m Keck I telescope. Each target field received simultaneous  $110 \times 3$  s integrations with the *g*-filter and  $60 \times 3$  s integrations with the *i*-filter using the blue and red arms of LRIS. A  $\sim 20''$  dither pattern was employed to generate on-sky flat field frames when incorporating all five fields. In addition, 1 s integrations were acquired in the *g*- and *i*-filters for photometric calibration of bright stars in each field. The seeing FWHM for the science exposures was  $\sim 0.8 - 0.9''$ . The data were reduced using IDL routines and combined and analysed using standard IRAF tasks.

## SMA observations

Observations of two H-ATLAS/SDP sources, ID81 and ID130, were obtained at  $880 \mu\text{m}$  using the only current high resolution submillimeter facility in the world, the SMA. The SMA is an interferometer located near the summit of Mauna Kea, Hawaii and consists of eight 6 m diameter radio telescopes. The two H-ATLAS sources were observed in Director's Discretionary Time (from February to May 2010) in three separate configurations, with baselines spanning a spatial range from 6 to 509 meters, over a total of 4 observing periods (Table S3).

Target observations from each period were interspersed with observations of calibration sources, quasars J0909+013 and J0825+031 (phase) and J0730-116 and J0854+201 (amplitude). The phase calibration targets were typically observed every 7 to 15 minutes, depending upon configuration (a faster cycle was used for the larger configurations). Calibration of the complex visibility data was performed within the SMA's MIR package, a suite of IDL-based routines designed for use with SMA data. The initial opacity correction was obtained through application of system temperature to the raw visibility data, a standard practice. Further complex gain corrections, to remove both atmospheric and instrumental amplitude and phase variations, were measured using the calibration quasars, which appear as point sources to the interferometer. Calibration of the absolute flux density scale was performed using measurements of Titan, whose continuum and line structure is known to within about 5% at sub-mm/millimeter wavelengths. The resulting calibrated visibility data for each source were combined and imaged within the NRAO Astronomical Image Processing System (AIPS). Photometry obtained for the SMA images along with those from PACS, SPIRE, MAMBO are given in table S1.

### **Plateau de Bure Interferometer observations**

The H-ATLAS/SDP sources ID81 and ID130 were observed in the CO J=3-2 and CO J=5-4 lines with the IRAM Plateau de Bure Interferometer (3). Both sources were observed in excellent atmospheric conditions and with the full sensitivity of the six-element array. The observing frequencies were based on the redshifts provided by the CSO/Z-spec spectrometer. The receiver bandwidth was adjusted for maximum sensitivity and the observing frequencies centered in the 1 GHz baseband of the narrowband correlator. Observations of ID81 were made on March 22, 2010 for an effective integration time of 22 min and 14 min, respectively, for the CO J=3-2 and J=5-4 lines. The RF calibration was measured on 3C84, and amplitude and phase calibrations were made on 0823+033. The J=3-2 and J=5-4 transitions in ID130 were observed on March 26 and April 16, 2010, respectively, for an effective integration time of 74 min and 32 min. The RF calibration was measured on 3C273, and amplitude and phase calibrations were made on 0906+015. The absolute flux calibration scales for ID81 and ID130 were established using as primary calibrator MWC349. Data reduction and calibration were made using the GILDAS software package in the standard antenna based mode.

### **Optical spectroscopic observations**

Optical spectroscopic observations of ID11 and ID17 were made using the ISIS double-arm spectrograph on the 4.2-m William Herschel Telescope (WHT). The R158B and R158R gratings were used to provide wavelength coverage across the entire optical spectrum,

split by a dichroic at  $\sim 5300 \text{ \AA}$ . Four 900-second exposures were taken of each source in a standard ‘ABBA’ pattern, nodding the telescope along the slit by 10 arcseconds between the first and second exposures, and back to the original position between the third and fourth integrations. This allowed initial sky subtraction to be performed by simply subtracting the ‘A’ frames from the ‘B’ frames. Additional sky subtraction was performed by subtracting the median value of each row, and then the positive and negative beams were aligned and coadded. Wavelength calibration was performed using observations of arc lamps taken with the same set-up. A one-dimensional spectrum was then optimally extracted. The spectra were taken through thin cloud and therefore no attempt has been made to flux-calibrate them. There was very little signal in the blue arms and so only the red-arm spectra are presented here. The redshifts of the two sources were determined by cross-correlation with template spectra. All reduction steps were undertaken using the IRAF package. The resulting spectra are shown in Fig. S3. The spectrum of ID11 reveals absorption lines associated to singly ionised calcium Ca H+K (rest-frame wavelengths:  $3968.5 \text{ \AA}$  for H-line and  $3933.7 \text{ \AA}$  for K-line) and the  $4000 \text{ \AA}$  break feature (rest-frame wavelength  $4000 \text{ \AA}$ ) at  $z = 0.793$ , while the spectrum of ID17 shows the emission from oxygen doublet [OII]3727 (rest-frame wavelengths  $3726\text{-}3729 \text{ \AA}$ ) and the  $4000 \text{ \AA}$  break feature at  $z = 0.944$ . In both spectra the absorption feature observed at  $\sim 7600 \text{ \AA}$  is due to the Earth’s atmosphere.

A 30-minute exposure of ID130 was taken on May 15, 2010, with the Apache Point Observatory’s 3.5-meter telescope and the DIS [Dual Imaging Spectrograph, (4)] long-slit spectrograph through medium clouds at an average airmass of 1.5. The spectrum was processed by subtracting the detector bias, dividing by a flat-field frame to correct for variable pixel response, performing distortion correction to align the spectrum in the wavelength and spatial directions, subtracting the sky flux determined from parts of the slit containing no sources, and applying a wavelength calibration by reference to emission lines from a Helium-Neon-Argon calibration lamp. Two emission lines in the spectrum (Fig. S4) were identified as [O II]3727 and [Ne III]3869 (rest-frame wavelengths  $3869 \text{ \AA}$ ) from the ratio of their observed wavelengths. From the ratio of their observed to emitted wavelengths the redshift of the galaxy was determined to be  $z = 0.2201 \pm 0.002$ .

## Modelling with GALFIT

GALFIT (5) is a publicly available two-dimensional non-linear fitting algorithm, which allows galaxy images to be modelled with one or multiple analytical light profiles. Each profile is constrained by a function and a set of parameters. GALFIT convolves the profiles with a user supplied point spread function, in this case empirical point spread functions constructed using nearby stars, and then performs a least-squares minimisation. No hard or soft constraints were applied to the fitting parameters to avoid any prior on the galaxy morphological type. For ID9 and ID11 single Sersic profiles resulted in a reduced  $\chi^2$  close to 1.0 (see table S4 for the best fit parameters). ID17 was fitted with two Sersic component, assuming two lensing galaxies. The resulting Sersic indices were both less than 1 (see table S4). For ID81 and ID130 two components were necessary to achieve a satisfactory fit, with a clean residual. The best fits were obtained using a combination of a compact elliptical Sersic core plus an exponential disk. No detectable background structure was revealed after subtracting the models, which shows the background galaxy is below the optical detection limit. Postage stamp images of ID9, ID11, ID17, ID81 and ID130 are shown in Figs S5 and S6, together with the corresponding best-fit models and residuals, while Fig. S7 shows the individual GALFIT components for ID81 and ID130. To derive photometric upper limits, we performed random aperture photometry on the i- and g-band Keck maps, using a 1.5 arcsecond radius. This radius was chosen to correspond with the structure visible in the SMA images for ID81 and ID130, which extends to regions with radii of approximately 1–1.5 arcseconds. The resulting flux distributions were fitted with Gaussians and the 3- $\sigma$  upper limits are presented in Table S4.

## Mass estimate from lensing

The Einstein radius of a strong galaxy-galaxy gravitational lens system can be measured from the configuration of multiple lensed images by averaging the distances of the images from the center of the lensing galaxy. For two of the H-ATLAS/SDP lens candidates, ID81 and ID130, the positions of the lensed images are constrained by high-resolution SMA follow-up imaging. The lensed images of the background sources appear as peaks in the SMA signal-to-noise ratio map. Here we have selected those peaks with signal-to-noise ratio above eight, which provided positions for four images in ID81 and two images in ID130. The error on the Einstein radius is estimated by taking into account the uncertainties on the position of the individual peaks. For a point source the rms error on its position is  $\sqrt{2}\sigma/\text{SNR}$  (assuming no systematic astrometry errors and uncorrelated Gaussian noise), where  $\sigma$  is the Gaussian rms width of the instrument beam ( $=\text{FWHM}/2\sqrt{2\ln 2}$ ), while SNR is the signal-to-noise ratio at the source position (6, 7). The SMA synthesised beam (derived by combining observations in VEX, COM and SUB configurations) has size  $0.81''\times 0.73''$  for ID81 and  $0.78''\times 0.72''$  for ID130. Therefore, in estimating the relative positional uncertainty of the peaks, we have assumed  $\text{FWHM}=0.75''$  and  $\text{FWHM}=0.77''$  for ID81 and ID130, respectively. The absolute positional uncertainty of the SMA images is estimated by referencing the data to nearby point-like sources (quasars) of known positions and is below 10 milli-arcseconds.

Once the Einstein radius is known, the mass within the Einstein ring can be easily derived assuming a Singular Isothermal Sphere (SIS) model (although the result is only little dependent on the model used) which is characterized by a projected surface density that falls off as  $\theta^{-1}$ , where  $\theta$  is the angular distance from the center of the mass distribution (8),

$$M_E = M(< \theta_E) = \pi \Sigma_{\text{crit}} \theta_E^2, \quad (1)$$

and  $\Sigma_{\text{crit}}$  is the *critical surface density*:

$$\Sigma_{\text{crit}} = \frac{c^2}{4\pi G} \frac{D_S}{D_L D_{LS}}. \quad (2)$$

In the equation above,  $c$  is the speed of light,  $G$  is the gravitational constant,  $D_L$  and  $D_S$  are the angular diameter distances to the lens and the source, respectively, while  $D_{LS}$  is the angular diameter distance between the lens and the source. The error on the mass is obtained by propagating the errors on the Einstein radius and on the spectroscopic/photometric redshifts used to derive the angular diameter distances. The estimated values of  $\theta_E$  and  $M_E$  are listed in Table 2.

## Gravitational lensing modeling

A detailed analysis of the lensed structure revealed by the SMA images is beyond the scope of this paper and is deferred to a forthcoming publication. However, in order to prove that such a structure is consistent with a lensing event, we have used the publicly available LENSMODEL software (9) to reproduce the positions of the peaks in the SMA maps. We have assumed a Singular Isothermal Ellipsoid (SIE) model (8) for the mass distribution of the lens galaxy. The SIE model consists of concentric and aligned elliptical isodensity contours with axis ratio  $q$ . The circular limit is the SIS model and corresponds to  $q = 1$ . The results are shown in Fig. S9. We have further assumed that the centroid of the mass model coincides with that of the light distribution of the lensing galaxy. The best-fit model for ID130 has ellipticity  $e = 0.16$  and position angle (measured East of North) of  $\theta = +75$  deg, consistent with the results found for the optical light-distribution that is dominated by the more compact Sersic profile (Table S4 and Fig. S8). For ID81, the mass distribution has ellipticity  $e = 0.24$  and position angle  $\theta = -3$  deg, which is not consistent with that measured for the luminous component (Table S4 and Fig. S8). Besides, the position of the peaks is not well reproduced by the model. This may hint at the effect of an external shear (which we did not include) due to a nearby cluster (photometrically detected 3.6 arcminutes away), in the direction indicated by the arrow in Fig. S9.

We have used the best-fit lens models to approximately quantify the magnification experienced by a background source described by a Gaussian profile with a Full Width at Half Maximum (FWHM) in the range 0.1-0.3". This extension is consistent with the physical size of the sub-mm galaxy studied by (10). The inferred magnification is  $\sim 18-31$  for ID81 and  $\sim 5-7$  for ID130. An example of lensed image, after convolution with the SMA point spread function, for the case FWHM=0.2" is shown in Fig. S9.

# Figures

Figure S 1: CO line detections in ID81 and ID130. The figure shows the difference between the spectrum of ID81 and that of ID130, derived from Zpectrometer observations. The relative spectrum is normalized such that the peak line strength of ID81 is equal to 1. In both objects the peak is associated with the CO J=1-0 emission line (rest-frame frequency 115.27 GHz).

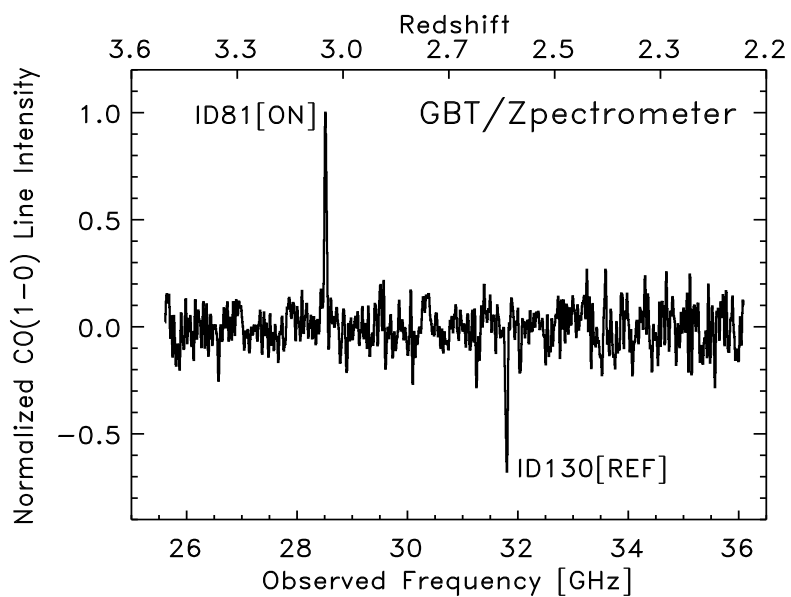


Figure S 2: CO line detections in ID9. The figure shows the spectrum derived from Z-Spec observations. The CO emission lines redshifted into the frequency range probed by Z-Spec correspond to transitions J=5-4 (rest-frame frequency 576.3 GHz) and J=6-5 (rest-frame frequency 691.5 GHz).

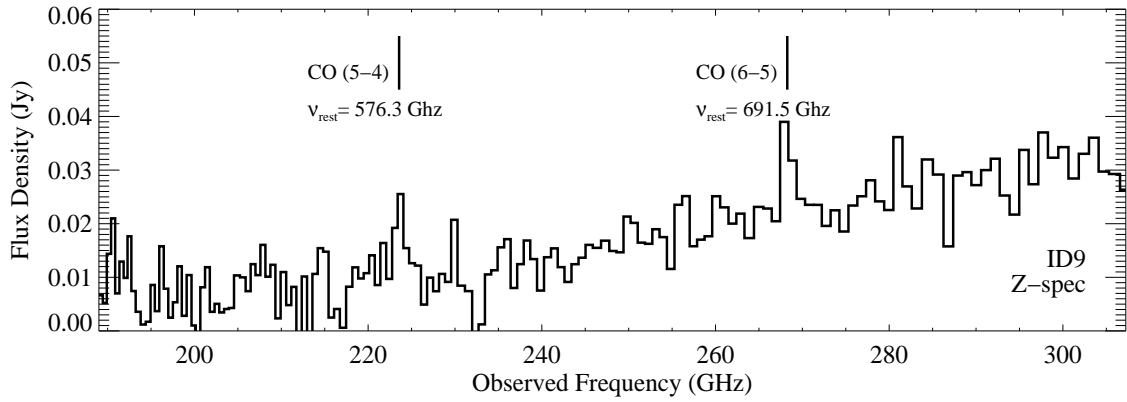


Figure S 3: Optical spectra of ID11 and ID17 obtained with the WHT.

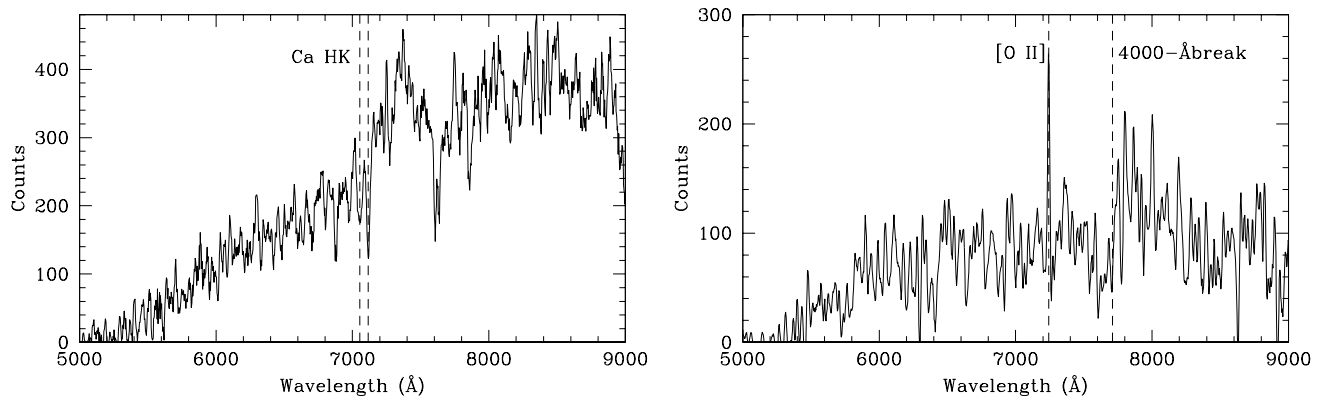


Figure S 4: Optical spectrum of ID130 obtained with the APO telescope. The bottom panel of the figure shows the reduced 2-d spectrum in the region of the detected emission lines. The top panel shows the flux summed in a 5-pixel wide (2 arcsecond) aperture centered on the object, with an arbitrary flux scale because the clouds made wavelength calibration impossible.

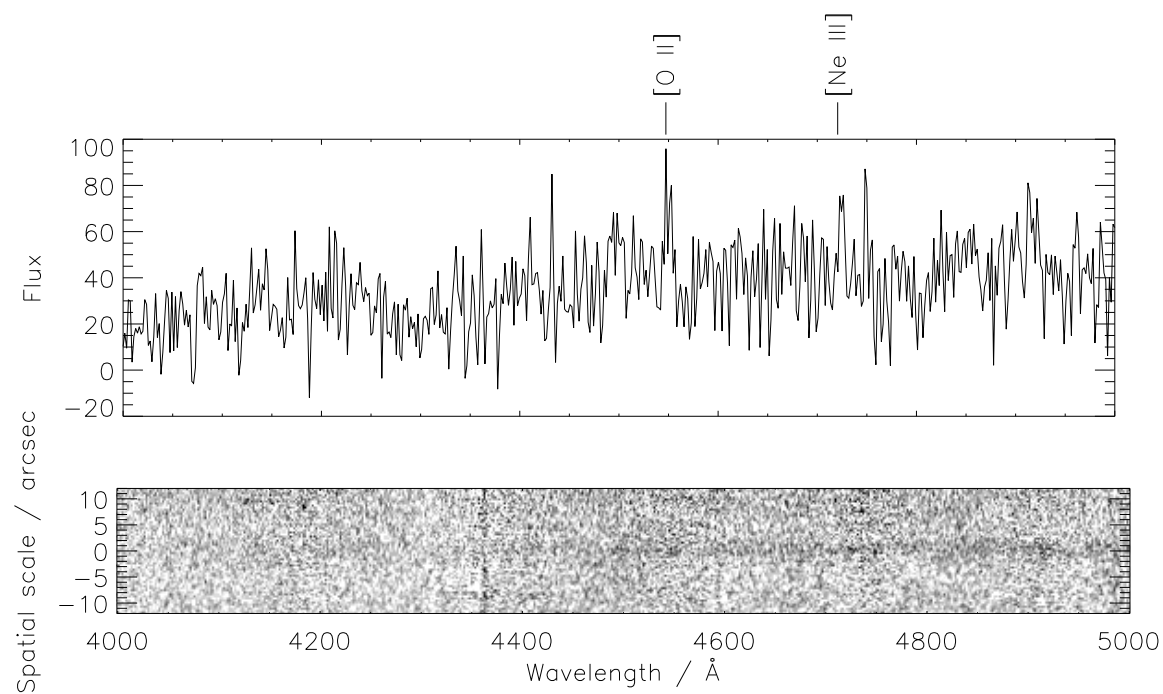


Figure S 5: Best-fit to the light distribution of the lens galaxy in the gravitational lens systems ID9, ID11 and ID17. The postage stamp images show, from left to right, the keck i-band image, the best-fit light distribution model provided by GALFIT and the residual map obtained by subtracting the best-fit model from the observed light distribution. The map of the residuals show no evident structure, implying that the background source is particularly faint in the optical, despite the magnification due to lensing.

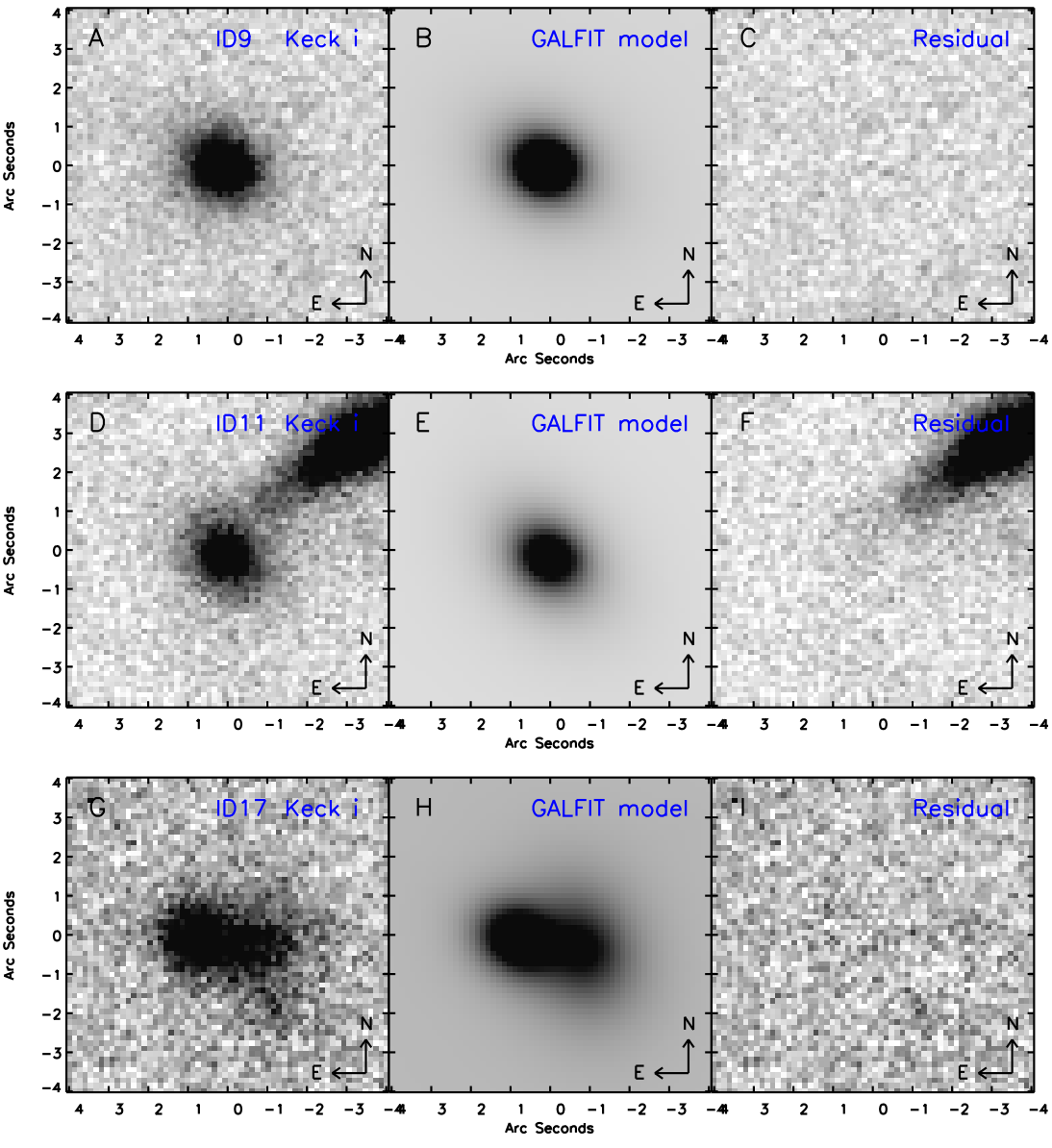


Figure S 6: Best-fit to the light distribution of the lens galaxy in the gravitational lens systems ID81 and ID130. The postage stamp images show, from left to right, the keck i-band image, the best-fit light distribution model provided by GALFIT and the residual map obtained by subtracting the best-fit model from the observed light distribution. The SMA contours (in red) are overlaid on the optical images (in steps of  $6\sigma$ ,  $8\sigma$ ,  $10\sigma$ , etc.) to highlight that there is no evident correspondence between the sub-mm and the optical emission in the residual maps.

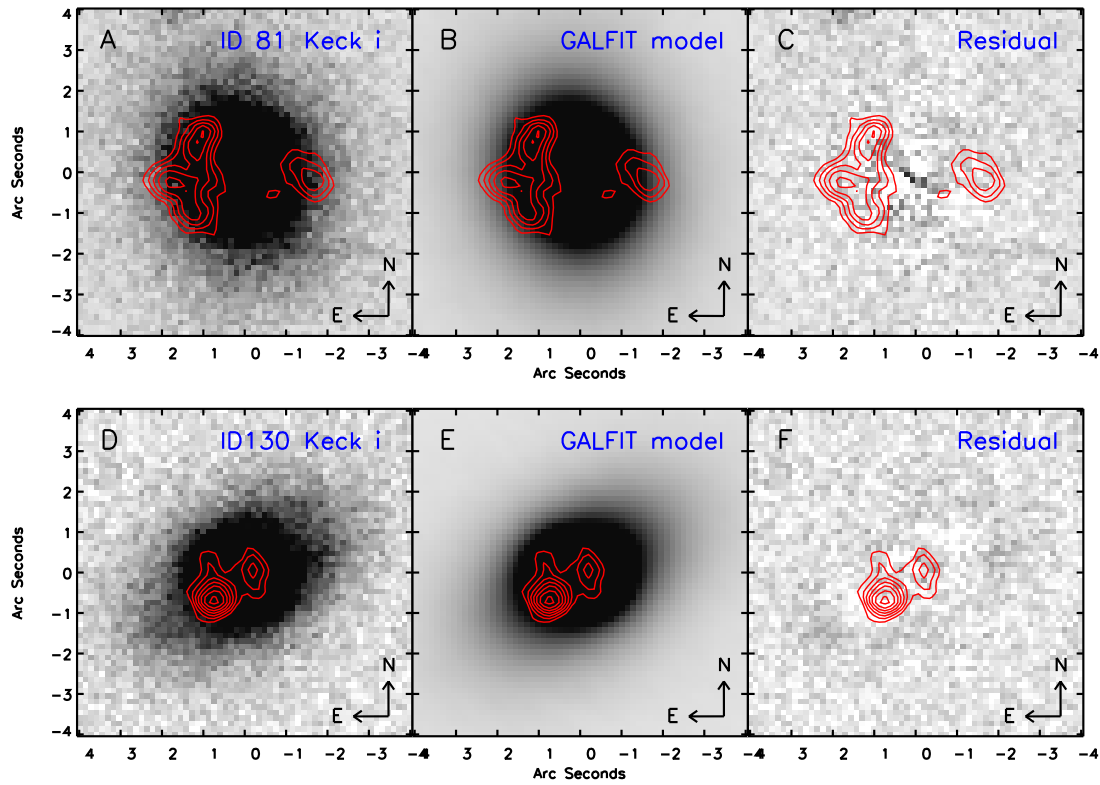


Figure S 7: Decomposition of the best-fit models of the lens galaxies in ID17, ID81 and ID130. *Top*: ID17 shows two partially superimposed components, indicative of two distinct lens galaxies, each described by a relatively shallow Sersic profile. *Middle*: ID81 has one single lens galaxy whose light profile is reproduced by the sum of a Sersic profile and an exponential disk profile. *Bottom*: ID130 is similar to ID81, with the light profile being described by the superposition of a compact Sersic profile and an exponential disk profile. In both ID81 and ID130, the SMA contours (in red) are overlaid on the optical images, in steps of  $6\sigma$ ,  $8\sigma$ ,  $10\sigma$ , etc.

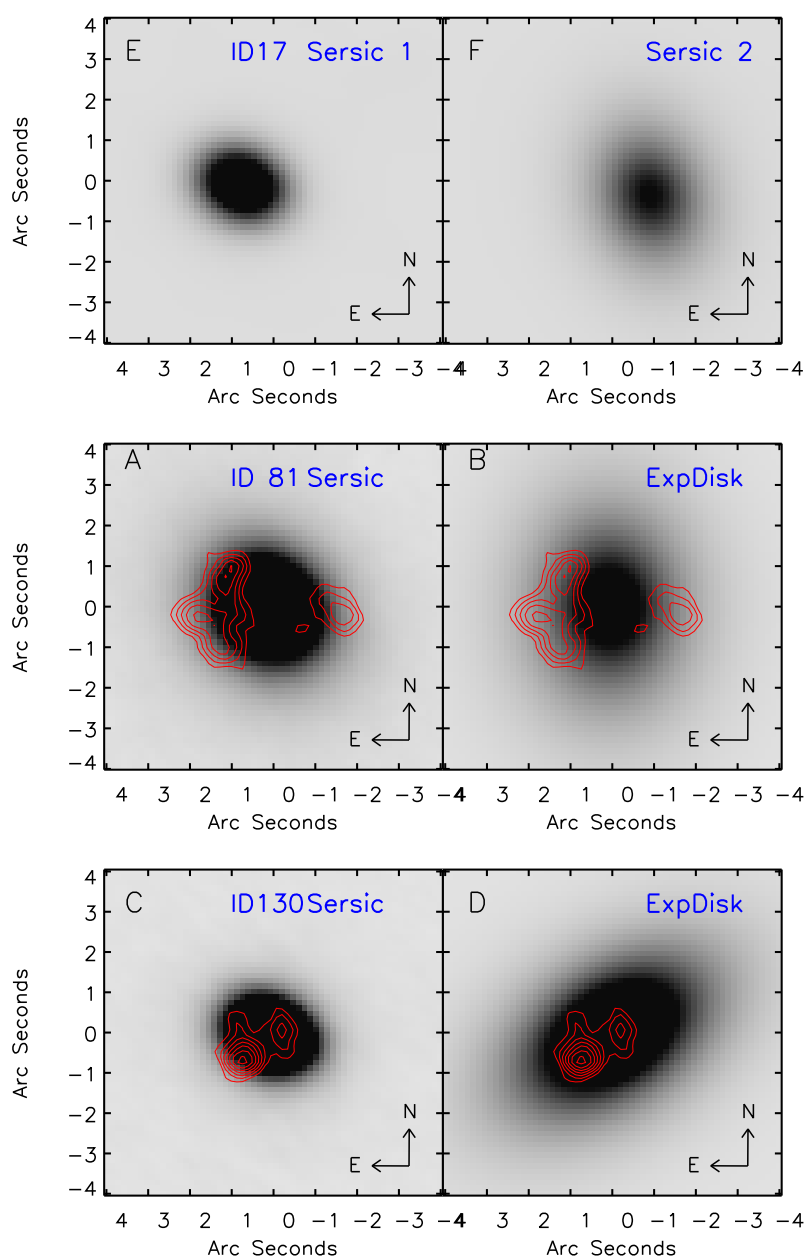


Figure S 8: Light profile of the lens galaxy in the gravitational lens systems ID81 and ID130. In both cases the best-fit to the observed light distribution of the lens galaxy is achieved using 2 components, i.e. an inner (more compact) Sersic profile and an exponential disk profile. These components are shown as a function of the distance from the galaxy center for ID81 (left-hand panel) and ID130 (right-hand panel).

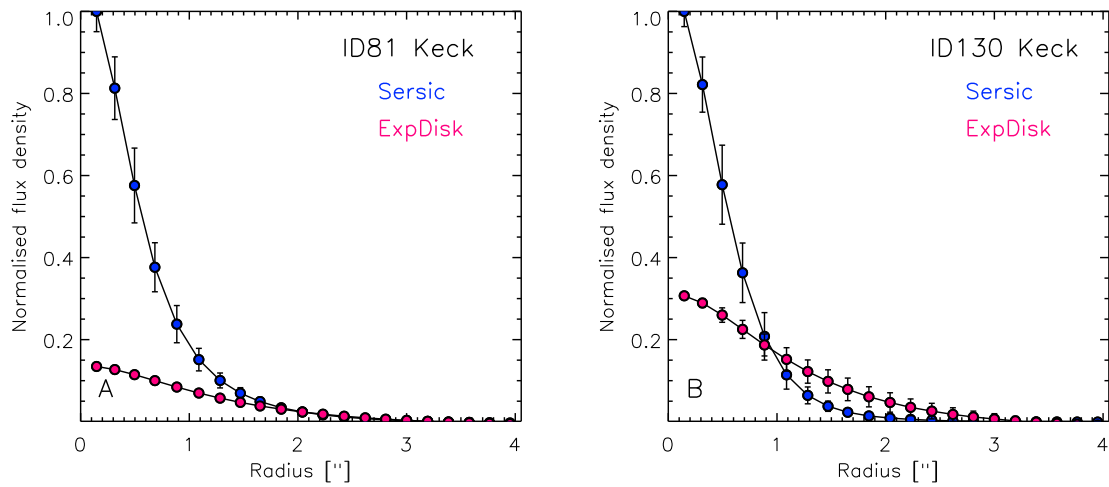
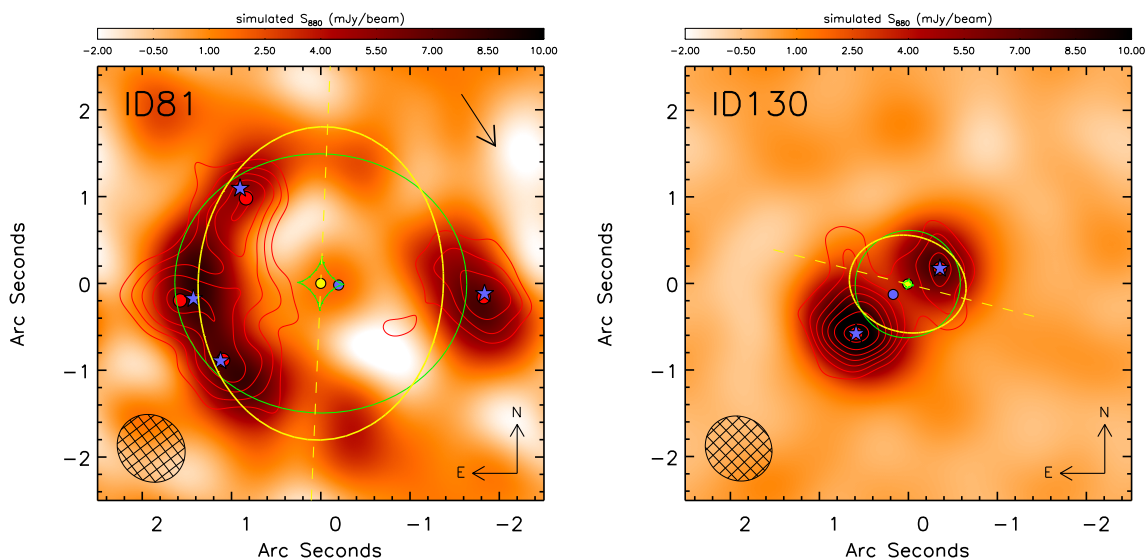


Figure S 9: Lens modelling of ID81 and ID130. The LENSMODEL software was used to fit the position of the peaks in the SMA images. A SIE model was assumed for the mass distribution of the foreground lenses. The image positions used in the fit are indicated by the red dots and correspond to the peaks in the SMA images (red contours in steps of  $6\sigma$ ,  $8\sigma$ ,  $10\sigma$  etc.). The blue stars are the best-fit positions of the lensed background source, assumed to be point-like. The best-fit position of the lens galaxy and of the background source are marked by the yellow and the blue dots, respectively. The caustic lines and critical lines of the best-fit lens model are indicated in green and yellow, respectively, while the yellow dashed line shows the major axis of the mass model. The simulated image shows the lensed image of a background source (after convolution with the SMA point spread function and added noise) described by a Gaussian profile with  $\text{FWHM}=0.2''$ .



# Tables

Table S 1: Sub-mm/millimeter fluxes for the lens candidates. The official H-ATLAS ID, according to IAU (International Astronomical Union) convention, is that derived from the position of the sources in the H-ATLAS SDP catalogue. The quoted errors on the *Herschel* flux densities include statistical errors, confusion noise and an absolute calibration uncertainty of 10 per cent for PACS/100 $\mu$ m, 20 per cent for PACS/160 $\mu$ m and 15 per cent for SPIRE.  $3\sigma$  upper limits at PACS wavelengths are provided when no detection is achieved at that significance level. Note that ID130 lies just outside the region covered by PACS. Fluxes at 880  $\mu$ m are from the SMA, while those at 1200  $\mu$ m are from the MAMBO array at the Institut de Radioastronomie Millimétrique (IRAM) 30 m telescope.

H-ATLAS ID	SDP ID	$S_{100}$ (mJy)	$S_{160}$ (mJy)	$S_{250}$ (mJy)	$S_{350}$ (mJy)	$S_{500}$ (mJy)	$S_{880}$ (mJy)	$S_{1200}$ (mJy)
H-ATLAS J090740.0-004200	9	187 $\pm$ 57	416 $\pm$ 94	485 $\pm$ 73	323 $\pm$ 49	175 $\pm$ 28	–	7.6 $\pm$ 0.8
H-ATLAS J091043.1-000321	11	198 $\pm$ 55	397 $\pm$ 90	442 $\pm$ 67	363 $\pm$ 55	238 $\pm$ 37	–	12.2 $\pm$ 1.2
H-ATLAS J090302.9-014127	17	78 $\pm$ 55	182 $\pm$ 56	328 $\pm$ 50	308 $\pm$ 47	220 $\pm$ 34	–	15.3 $\pm$ 1.3
H-ATLAS J090311.6+003906	81	$\leq$ 62	$\leq$ 83	129 $\pm$ 20	182 $\pm$ 28	166 $\pm$ 27	76.4 $\pm$ 3.8	20.0 $\pm$ 0.7
H-ATLAS J091305.0-005343	130	–	–	105 $\pm$ 17	128 $\pm$ 20	108 $\pm$ 18	39.3 $\pm$ 2.3	11.2 $\pm$ 1.2

Table S 2: UV/optical/NIR photometry for the lens candidates. UV data are from GALEX, optical photometry is from SDSS and NIR data are from UKIDSS [as reprocessed by GAMA; (11)]. Where photometric measurements are not listed it means that the source is not covered at those wavelengths. The  $3\text{-}\sigma$  upper limits shown within parenthesis for the UKIDSS wavelengths are obtained from the residual image after the best-fit GALFIT model of the source has been subtracted off. These limits are used to constrain the SED of the background source.

SDP ID	9	11	17	81	130
GALEX FUV ( $\mu\text{Jy}$ )	-	-	-	$0.23\pm 0.18$	-
GALEX NUV ( $\mu\text{Jy}$ )	-	-	-	$1.9\pm 1.1$	-
SDSS u ( $\mu\text{Jy}$ )	$0.24\pm 0.23$	$0.57\pm 0.59$	$3.3\pm 1.6$	$3.9\pm 2.0$	$1.7\pm 1.7$
SDSS g ( $\mu\text{Jy}$ )	$1.79\pm 0.43$	$1.01\pm 0.45$	$3.9\pm 6.4$	$24.9\pm 1.1$	$19.41\pm 0.72$
SDSS r ( $\mu\text{Jy}$ )	$5.81\pm 0.70$	$3.94\pm 0.65$	$7.7\pm 1.0$	$114.8\pm 2.1$	$66.1\pm 1.2$
SDSS i ( $\mu\text{Jy}$ )	$14.9\pm 1.1$	$11.3\pm 1.0$	$15.3\pm 1.5$	$197.7\pm 3.6$	$108.6\pm 2.0$
SDSS z ( $\mu\text{Jy}$ )	$27.0\pm 3.7$	$21.5\pm 4.2$	$11.8\pm 6.0$	$278.0\pm 3.6$	$143.2\pm 6.6$
UKIDSS Y ( $\mu\text{Jy}$ )	-	-	$27.7\pm 9.5(<6.6)$	$321.3\pm 3.2(<6.3)$	-
UKIDSS J ( $\mu\text{Jy}$ )	-	$102.4\pm 9.8(<16)$	$56\pm 17(<12)$	$367\pm 11(<9.2)$	-
UKIDSS H ( $\mu\text{Jy}$ )	$73\pm 15(<5.0)$	$237\pm 17(<14)$	$107\pm 19(<8.2)$	$508.1\pm 5.3(<8.5)$	-
UKIDSS K ( $\mu\text{Jy}$ )	$132\pm 24(<6.5)$	-	$108\pm 23(<9.7)$	$573.7\pm 6.2(<14)$	-

Table S 3: Technical information on the SMA follow-up observations. This includes: the date the measurements were taken (Date), the configuration of the antennas (Conf.; VEX=‘very-extended’, SUB=‘sub-compact’, COM=‘compact’), the number of antennas used (Nant.), the projected baselines lengths (min/mean/max Pr Baselines), the Local Oscillator Frequency (LO Freq.), and the on–source integration time (Int. time).

SDP ID	Date	Conf.	Nant.	min/mean/max Pr Baselines (m)	LO Freq. (GHz) <sup>a</sup>	Int. time (min)
81	25Feb10	VEX	7	69/281/509	340.7	289
130	28Feb10	VEX	7	76/289/509	340.7	298
81	16Mar10	SUB	5	6/ 17/ 25	340.7	144
130						152
81	09Apr10	COM	6	9/ 38/ 69	341.6	153
130						144

<sup>a</sup>Total bandwidth coverage is LO-8 to LO-4 (LSB) and LO+4 to LO+8 (USB) for a total of 8 GHz. The small difference in LO Frequency between compact configuration observations and the subcompact and very extended observations is not important in this context.

Table S 4: GALFIT results for the five gravitational lens systems. The  $3\text{-}\sigma$  upper limits given are for an extended source and derived from the distribution of 1.5 arcsecond radius aperture photometry of the Keck maps.

H-ATLAS ID	profile <sup>a</sup>	$\chi^2_\nu$ <sup>b</sup>	radius <sup>c</sup> (arcsec)	$\delta$ <sup>d</sup>	Axis ratio	Angle <sup>e</sup> deg.	g- $3\sigma$ ( $\mu\text{Jy}$ )	i- $3\sigma$ ( $\mu\text{Jy}$ )
9	Sersic	1.07	0.85	5.36	0.72	56.76	0.162	0.641
11	Sersic	1.03	1.10	2.97	0.65	39.61	0.229	0.442
17	Sersic	1.07	0.61	0.54	0.71	63.25	0.202	0.404
	Sersic	—	1.36	0.91	0.69	12.83	—	—
81	Sersic	1.13	0.70	2.82	0.78	36.45	0.130	0.202
	ExpDisk	—	1.20	—	0.72	0.62	—	—
130	Sersic	1.00	0.32	1.23	0.52	56.82	0.198	0.351
	ExpDisk	—	1.11	—	0.55	-54.64	—	—

<sup>a</sup>ExpDisk = exponential disk profile

<sup>b</sup>Reduced  $\chi^2$

<sup>c</sup>Radius for Sersic and disk scale length for ExpDisk

<sup>d</sup>Sersic index

<sup>e</sup>Angle measured east of north

## References and Notes

1. J. B. Oke, *et al.*, *Publ. Astron. Soc. Pac.* **107**, 375 (1995).
2. J. K. McCarthy, *et al.*, *Society of Photo-Optical Instrumentation Engineers (SPIE) Conference*, S. D'Odorico, ed. (1998), vol. 3355, pp. 81-92
3. S. Guilloteau, *et al.*, *Astron. & Astrophys.* **262**, 624 (1992)
4. <http://www.apo.nmsu.edu/arc35m/Instruments/DIS/>
5. C. Y. Peng, L. C. Ho, C. D. Impey, H. Rix, *Astron. J.* **124**, 266 (2002)
6. J. J. Condon, *Publ. Astron. Soc. Pac.* **109**, 166 (1997)
7. R. J. Ivison, *et al.*, *Mon. Not. R. Astron. Soc.* **380**, 199 (2007)
8. R. Kormann, P. Schneider, M. Bartelmann, *Astron. & Astrophys.* **284**, 285 (1994)
9. C. R. Keeton, *available at <http://xxx.lanl.gov/abs/astro-ph/0102340> (2001)*
10. A. M. Swinbank, *et al.*, *Nature* **464**, 733 (2010)
11. D. Hill, *et al.*, *available at <http://xxx.lanl.gov/abs/astro-ph/1009.0615>*